An Innovative Islanding Detection Algorithm for Grid-Tied Inverter Utilizing In-Circuit Magnetic Characteristics of Inductors in LCL Filters

Shanthi Kumar N B, Sreedhar MADICHETTY, Chandrakala PANNELA, Pradeep KUMAR, and Mahmood SHAIK

***Abstract*—Unintentional islanding in grid-connected photovoltaic inverters (GCPVI) poses a significant challenge to power system reliability and safety. This article introduces a novel islanding detection method that leverages the magnetic characteristics of the GCPVI system. The *BH* curve, which defines the relationship between the magnetic flux density (*B*) and the magnetic field strength (*H*), is derived from the voltage across the inverter-side and grid-side inductors, and the current flowing through them. These *BH* curves are obtained for each cycle of the measured signals and analysed over successive cycles to calculate the alienation coefficient and cumulative index. The computed coefficients and indices form a time series vector, referred to as the islanding index. This index is compared against a threshold to detect unintentional islanding, even in the non-detection zone (NDZ). The proposed algorithm is experimentally validated on a single-phase hardware-based grid-connected inverter driven by bipolar pulse-width modulation. The measured voltage and current samples of the both side inductors are transmitted to a micro controller for real-time analysis. Using these samples, the method effectively distinguishes islanding from non-islanding events, such as load switching and distributed generation (DG) tripping, within a shorter time frame, adhering to international standards.**

***Index Terms*—Alienation coefficient, *BH* curve, cumulative index, grid connected inverter, islanding, non-islanding.**

I. Introduction

GRID-CONNECTED photovoltaic inverters (GCPVIs) convert the direct current (DC) output from solar panels into alternating current (AC) that can be fed into the electrical grid by matching the grid's voltage, frequency, and phase. These inverters play a crucial role in the seamless integration of solar-generated electricity into the grid. Islanding is a phenomenon where a portion of the electrical grid becomes isolated but continues to generate power. This condition poses significant safety risks to utility workers and the general public. Detecting islanding is critical to ensuring the safety, stability, and reliability of grid-connected PV systems. By promptly identifying and disconnecting during islanding events, PV systems can mitigate safety risks, protect equipment, comply with regulations, and support the seamless integration of renewable energy into the electrical grid [1].

Many international islanding standards have been formulated to provide guidelines for safe operation of the grid. Some of the widely used islanding detection standards include UL 1741 (Underwriters Laboratories Inc.), IEEE 1547 [2], IEC 62116 (International Electro technical Commission), IEEE 929 [3], VDE 0126-1-1 (German Standard), AS 4777.3-2005 (Australian Standard), as well as the Korean and Japanese standards [4]. The detection time requirements for islanding, along with the voltage and frequency limits specified by various international standards, are compared in Table I. Here, V_n and f_n represent the nominal voltage and nominal frequency, respectively.

The principle of using *BH* (magnetization) curves for islanding detection relies on the non-linear magnetic characteristics of inductive components in power systems, such as transformers and inductors. The *BH* curve represents the relationship between magnetic flux density (*B*) and magnetic field strength (*H*), exhibiting non-linear behavior, particularly near the saturation region. During normal grid operation, voltage and current waveforms maintain a predictable pattern governed by these magnetization characteristics. However, when an islanding event occurs, there is a sudden change in load dynamics, causing variations in the system's voltage, current, and impedance. These changes affect the operating point of magnetic components on the *BH* curve, leading to noticeable shifts in harmonic content and inductive response. The saturation effects of the core result in increased harmonic distortion, especially in the second and third harmonic components, which can serve as a reliable indicator of islanding. By continuously monitoring deviations in inductance, flux behavior, and harmonics, an islanding condition can be detected with high accuracy. The primary advantage of this method is that it provides a passive, non-intrusive means of detection without requiring active signal

Manuscript received July 23, 2024; revised December 18, 2024 and January 30, 2025; accepted February 16, 2025. Date of publication March 30, 2025; date of current version February 25, 2025. This work was supported by Science and Engineering Research Board, Department of Science and Technology, Ministry of Science and Technology, India, under the grant PDF/2023/000631. *(Corresponding author: Sreedhar Madichetty.)*

All authors are with Department of Electronics and Computer Engineering, Ecole Centrale School of Engineering, Mahindra University, Hyderabad 500043, India (e-mail: shanthi21peee001@mahindrauniversity.edu.in; sreedhar.803@gmail.com; se23maev005@mahindrauniversity.edu.in; pradeepkumarrao110@gmail.com; shaik.1@iitj.ac.in).

Digital Object Identifier 10.24295/CPSSTPEA.2025.00008

TABLE I
INTERNATIONAL ISLANDING DETECTION STANDARDS

Standards	Islanding Detection Time	Acceptable Frequency Range	Acceptable Voltage Range
UL 1741, IEEE 1547, IEEE 929	IDT < 2 s	59.3 Hz $\leqslant f_n \leqslant$ 60.5 Hz	88% of $V_n \leqslant V_n \leqslant$ 110% of V_n
IEC 62116	IDT < 2 s	f_n – 1.5 Hz $\leqslant f_n$; $f_n \leqslant f_n$ +1.5 Hz	85% of $V_n \leqslant V_n \leqslant$ 115% of V_n
VDE 0126-1-1	IDT < 0.2 s	47.5 Hz $\leqslant f_n \leqslant$ 50.2 Hz	80% of $V_n \leqslant V_n \leqslant$ 115% of V_n
Korean Standard	IDT < 0.5 s	59.3 Hz $\leqslant f_n \leqslant$ 60.5 Hz	88% of $V_n \leqslant V_n \leqslant$ 110% of V_n
AS4777.3-2005	IDT < 2 s	Setting Value	Setting Value
Japanese Standard	IDT < 0.5 s	Setting Value	Setting Value

injection. Additionally, it enables fast response times, making it a practical solution for real-time monitoring. However, the approach must be fine-tuned for specific system configurations, as external disturbances and variations in system impedance may influence detection accuracy. Combining *BH* curve analysis with advanced digital signal processing (DSP) techniques or integrating it with other islanding detection methods can further enhance its effectiveness. Overall, leveraging the nonlinear magnetization properties of inductive elements presents a promising and efficient technique for islanding detection, ensuring the safe and stable operation of distributed generation systems.

A. Literature Review

Various detection techniques are proposed, encompassing local control, remote control, artificial intelligence, and signal processing techniques. Remote-control methods, such as PLCC, SCADA, and transfer trip, provide highly reliable islanding detection by eliminating the non-detection zone (NDZ). However, these methods are cost-prohibitive and impractical for smaller systems due to extensive infrastructure requirements. Signal processing techniques, including Fourier and Wavelet transforms, analyse time and frequency-domain variations in voltage and current. While they offer precision, these methods demand sophisticated hardware, and significant computational resources, and still struggle to eliminate NDZ issues. Computational intelligence techniques, such as ANN, SVM, and ANFIS deliver high accuracy and adaptability to complex grid configurations but are computationally intensive, require large training datasets, and introduce implementation intricacies [5]. Remote-control methods lack localized monitoring of parameters like voltage and frequency, necessitating the adoption of local-control techniques for effective islanding detection. Local control methods are further categorized into active, passive, and hybrid techniques. Active methods inject disturbances at the point of common coupling (PCC) to detect grid disconnection, providing high reliability but degrading power quality and encountering challenges in multi-inverter setups. Hybrid methods combine active and passive approaches to enhance accuracy and minimize NDZ, but they impact power quality and exhibit significant complexity in large-scale system implementations [6]. This article primarily focuses on reviewing passive methods, where the primary challenge lies in detecting islanding within the NDZ. Several methods have been proposed to address this issue by enabling detection within a few cycles of islanding inception. One proposed method monitors the rate of change of kinetic energy over reactive power (ROCOKORP) [7], which calculates a novel index based on the kinetic energy of distributed generators (DGs). However, this method relies on accurate parameter estimation and involves potential computational complexity in dynamic grid scenarios. Another approach combines passive low-threshold settings with active three-phase static RC load activation [8], aiming to eliminate the NDZ. The complexity of this method lies in optimizing threshold settings and load configurations to ensure accurate detection while avoiding misoperations during non-islanding events. The passive communication-based technique in [9] leverages phase angle differences of superimposed impedance at DG and PCC ends via fast communication links. While effective, it depends on secure communication channels that may experience delays or failures under adverse network conditions. A multi-SOGI-based passive detection method [10] extracts harmonic signatures for virtual impedance calculation but suffers from dependency on accurate harmonic data, high computational requirements, and reduced effectiveness in distorted or dynamic grids. Another passive algorithm [11] utilizes the rate of change of potential energy as an index, achieving nearly zero NDZ, but faces sensitivity to noise in frequency and ROCOF calculations, reliance on precise parameter estimation, and potential computational inefficiency in dynamic conditions. In [12], an adaptive ROCOF-based technique dynamically calculates frequency and ROCOF using PLL settings, reducing NDZ to zero. However, it relies heavily on precise PLL configurations, exhibits sensitivity to transient disturbances, and encounters delays in frequency tracking during rapid grid changes, along with scalability challenges in complex microgrids. Similarly, the μPMU-based islanding detection method in [13] achieves zero NDZ by monitoring voltage and current phasors. Despite its effectiveness, it relies on precise measurements, and high-resolution data, and is sensitive to noise and disturbances, making it economically unviable for widespread implementation. Furthermore, directly monitoring the operating point may not reliably detect islanding, especially in the non-detection

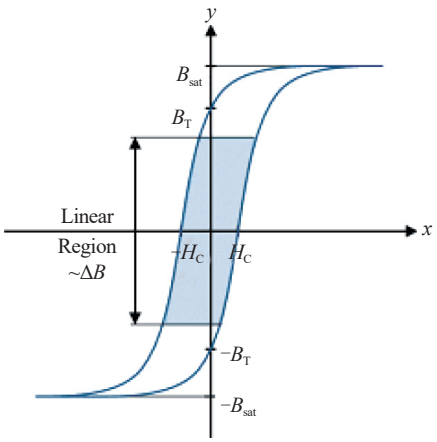

Fig. 1. *BH* characteristics of a magnetic material.

zone (NDZ), where variations are minimal. In contrast, the *BH* curve provides deeper insight into magnetic characteristics, capturing subtle changes in inductance, flux, and harmonic distortion. Unlike voltage and frequency, which can remain stable, core saturation and flux behavior shift noticeably when the grid is lost. By analyzing alienation and correlation indices from successive *BH* curves, islanding can be detected even in conditions where traditional methods fail.

To overcome all the drawbacks discussed in the literature, this article proposes a novel islanding detection method using the magnetic characteristics (*BH* curves) derived from the current through the grid-side and inverter-side filter inductors, as well as the voltage across them. *BH* curves provide valuable insights into the magnetic behavior of grid-connected PV inverters and serve as a foundation for developing effective islanding detection techniques to enhance the reliability and safety of grid-connected renewable energy systems.The *BH* curves obtained over successive cycles are converted into gray scale images and compared to calculate the alienation coefficients [14]. These coefficients are used to compute an index, which is then compared against a threshold to detect islanding events. The proposed algorithm successfully detects islanding within the time limits prescribed by various international standards.

B. Organization

The rest of the paper is organized as follows: Section II discusses the BH curves in detail, including their mathematical analysis and potential application in islanding detection. Section III presents the test system discussion. Section IV elaborates on the proposed algorithm. Section V discusses the results, including the thresholds and a comparison of the outcomes, with the conclusion presented in Section VI.

II. *BH* Curves

A. About BH Curves

BH curves, also known as hysteresis loops, graphically represent the variation between the magnetic flux density (B) and the magnetic field strength (H) in a magnetic material. They are widely used in the field of magnetism and in electromagnetic devices such as transformers, inductors, and magnetic sensors. The theory behind *BH* curves is rooted in the behavior of magnetic materials when subjected to an external magnetic field. When a magnetic material is exposed to a magnetic field, it becomes magnetized, with its magnetic domains aligning in the direction of the applied field. The relationship between the magnetic flux density (B) and the magnetic field strength (H) during this process is plotted on a graph, resulting in a hysteresis loop, as illustrated in Fig. 1.

As the magnetic field strength (H) increases, the magnetic flux density (B) increases proportionately until the material reaches saturation. At this point, the proportional increment of B ceases, and the curve becomes flat at the edges, corresponding to B_{sat}. When the magnetic field strength (H) is reduced to zero, the flux density (B) does not return to zero. Instead, the magnetic material retains some residual magnetism, a property known as remanence B_r. To remove the magnetism ($B = 0$) from the magnetic material, the magnetic field strength (H) must be applied in the reverse direction until it reaches H_c on the x-axis. This value represents the coercivity of the magnetic material. The phenomenon of saturation is similarly observed in the reverse direction.

B. Potential of BH Curves for Islanding Detection

The potential application of *BH* curves for islanding detection in grid-connected PV systems lies in their ability to capture changes in the magnetic properties of components such as transformers or inductors during islanding events. Grid-connected PV systems typically include magnetic components like transformers and inductors, which play critical roles in power conversion and distribution. These components exhibit specific magnetic properties characterized by *BH* curves. During normal grid-connected operation, the magnetic properties of these components remain relatively stable. However, when an islanding event occurs and the grid becomes isolated, the operating conditions of the PV system and its connected components may change. These changes can affect the magnetic properties of the components, leading to alterations in their *BH* curves. Variations in load conditions, solar irradiance, or grid parameters during islanding events can induce changes in magnetic flux density (B) or magnetic field strength (H), resulting in shifts or distortions in the *BH* curves.

Monitoring the *BH* curves of critical components in real-time enables the detection of abnormal changes that indicate islanding conditions. Deviations from the expected *BH* curve characteristics can signal the presence of islanding and trigger appropriate protective measures. Overall, *BH* curve analysis offers a novel approach to islanding detection in grid-connected PV systems by leveraging the magnetic properties of system components and serves as a primary motivation for this work.

C. Mathematical Analysis to Obtain BH Curve

The *BH* curve of an inductor is obtained from the measured

values of the voltage $V(i)$ and the current $I(i)$ through it. The *BH* curve [15] for the k_{th} cycle is obtained from the following steps:

Obtain the mean voltage $V_{mean,k}$

$$V_{mean,k}=\frac{1}{q}\sum_{i}^{q}V(i) \tag{1}$$

where $i = 1, 2, .., q$ samples.

Compute the normalized voltage waveform $V_k(t)$ by subtracting $V_{mean,k}$

$$V_k(t)=V(i)-V_{mean,k} \tag{2}$$

Perform continuous integration of the voltage waveform to obtain the magnetic flux at each data sample over the entire cycle *k*.

$$\phi_k(t)=\int V_k(t)\mathrm{d}t \tag{3}$$

Calculate the magnetic flux density $B_k(t)$

$$B_k(t)=\frac{\phi_k(t)}{N\cdot S} \tag{4}$$

where, N and S are the number of turns and the toroidal area of cross section.

Normalize the flux density to obtain only the changes in the flux density by finding the mean flux density $B_{mean,k}$ is obtained as

$$B_{mean,k}=\frac{1}{q}\sum_{i}^{q}B_k(i) \tag{5}$$

Compute the normalized flux density as

$$B_{n,k}(t)=B_k(t)-B_{mean,k} \tag{6}$$

Determine the DC flux density which determines the operating point of the transformer or inductor in an in-circuit operation as $B_{dc,k}$ and given by

$$B_{dc,k}=\frac{L_k\cdot I_{ave,k}}{S} \tag{7}$$

where, L_k , $I_{ave,k}$ are the inductance and the average value of the current. The value of inductance is computed as the ratio of the integral of voltage data to current data, given by

$$L=\frac{\int e\,\mathrm{d}t}{I} \tag{8}$$

Obtain the magnetic flux density vector $B_{kf}(t)$ as

$$B_{kf}(t)=B_{dc,k}+B_{n,k}(t) \tag{9}$$

Obtain the magnetic field strength H data by

$$H_k(t)=\frac{I_k(t)\cdot N}{ml} \tag{10}$$

where, N, ml are the number of turns and the length of the magnetic path respectively which are given as input based on the inductor physical data.

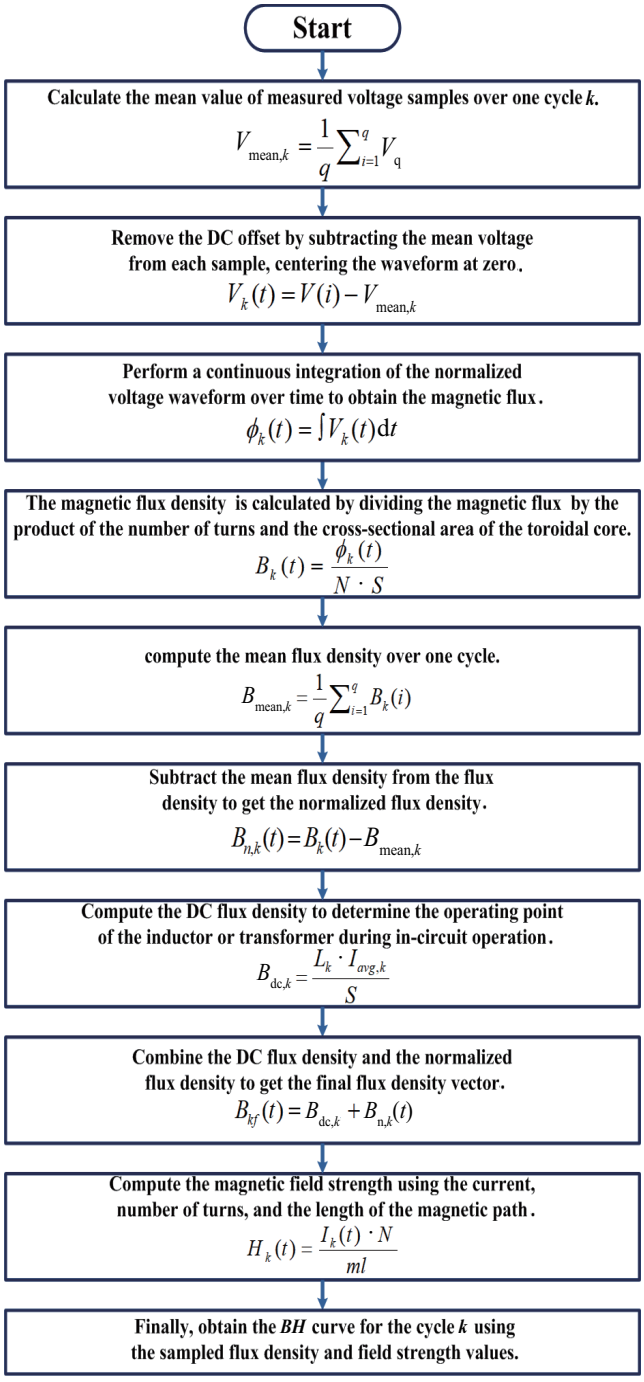

Fig. 2. Flow chart to obtain BH curve

This process is repeated for all number of cycles from the acquired data. The flowchart in Fig. 2 illustrates the step-by-step procedure for obtaining the *BH* curve in a real-time application.

D. Correlation and Alienation Coefficients of BH Curves

The correlation coefficient measures the similarity between two patterns. Correlation coefficient (R) of two dimensional

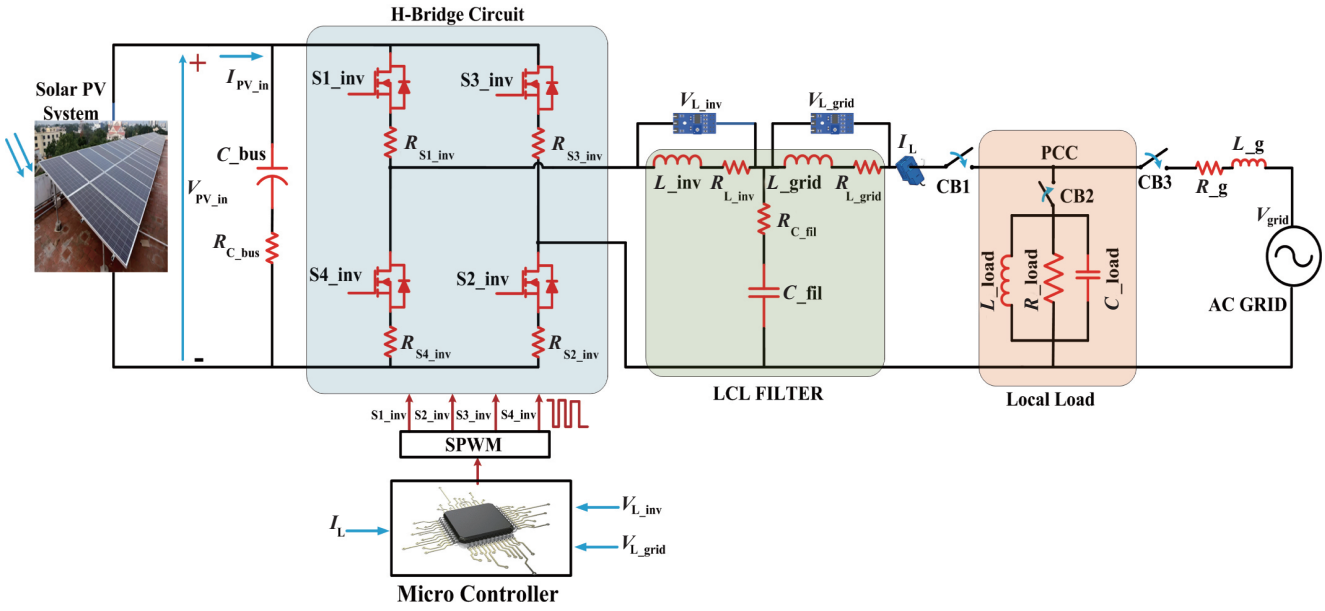

Fig. 3. block diagram of the proposed system.

matrices M and N of size $p \times q$ is shown in (11).

$$R(M,N)=\frac{\sum_p \sum_q (M_{pq}-\overline{M})(N_{pq}-\overline{N})}{\sqrt{\left[\sum_p \sum_q (M_{pq}-\overline{M})^2\right]\left[\sum_p \sum_q (N_{pq}-\overline{N})^2\right]}} \quad (11)$$

where, $\overline{M}$ and $\overline{N}$ are the mean of the matrices. The measure of uncorrelated patterns can be obtained by alienation coefficient

$$A(M,N)=1-R^2(M,N) \quad (12)$$

The *BH* curve obtained is converted into a two-dimensional matrix of size $p \times q$ (gray scale image). The matrices corresponding to islanding and non-islanding patterns must have the same size. If the patterns are exactly the same then $R = 1$ and $A = 0$ and if the patterns are completely different, then $R = 0$ and $A = 1$. Thus, the values of alienation and correlation coefficients can vary between 0 and 1.

E. Threshold Criteria

The feature vector, which includes the alienation coefficient, the ratio of alienation and correlation index, and the cumulative index, is obtained both before and after the islanding event. The absolute maximum value post-islanding or disturbance, calculated for a half cycle or quarter cycle, is selected as the islanding index. Islanding indices are computed from the feature vectors for various cases, such as *R*-load, *RL*-load, and variations in *P* and *Q*. The minimum value of all the islanding indices is defined as the "Islanding index-min," which equals the minimum of the absolute maximum values from the half cycle after islanding across all islanding cases. Similarly, the absolute maximum value (or islanding index) is also obtained for non-islanding events, such as load switching or capacitor switching. The maximum value of these indices is referred to as the "Islanding index-max". For normal cases, the same half-cycle post-disturbance time is considered, and the absolute maximum value is calculated. Thus, Islanding index-max is defined as the maximum absolute value from the half cycle after disturbances in non-islanding cases. The threshold is determined by taking the average of Islanding index-min and Islanding index-max. Therefore, the threshold is approximately calculated as

$$\frac{Islandingindex\text{-}min+Islandingindex\text{-}max}{2} \quad (13)$$

III. Test System Considered

The proposed scheme is thoroughly tested, and its complete methodology is depicted in Fig. 3. The block diagram illustrates a single-phase grid-connected PV system that supplies power to both local loads and the grid. The system comprises an H-bridge inverter and LCL filters, which together form a crucial part of the grid-connected PV configuration. This system is connected to local loads via circuit breakers CB1 and CB2, and to the grid via CB1 and CB3, ensuring flexibility and control in power distribution. Voltage and current sensors are strategically installed on the inductors on both the inverter side (L_{inv}) and the grid side (L_{grid}) of the LCL filter to monitor the voltage across and the current through these inductors in real-time. Data collection is performed under various operating conditions, including before islanding (normal grid-connected mode), after islanding (when the grid becomes isolated due to an islanding event), DG tripping (when distributed generation sources disconnect), and load switching (when local loads are added or removed, causing transient changes in system behaviour). The collected data is transmitted to a micro controller for detailed analysis, where voltage and current signals are processed to extract key features, such as changes in magnetic properties represented through variations in the *BH* curves. The

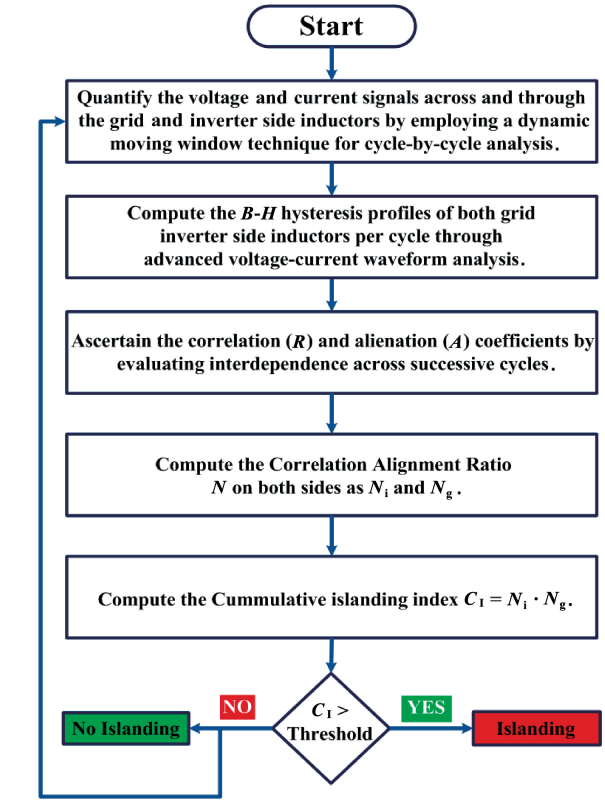

Fig. 4. Flow chart of the proposed algorithm.

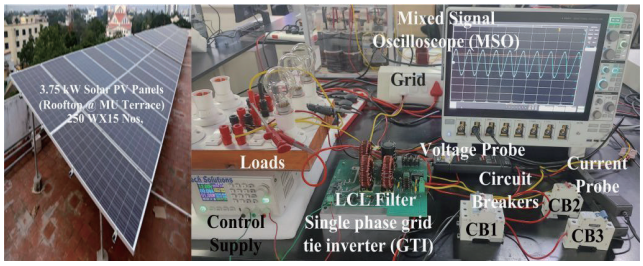

Fig. 5. Real-time implementation of 3.75 kW grid-connected PV system and its field test of proposed methodology.

micro controller applies the proposed algorithm to detect deviations in the patterns, enabling the identification of islanding events and distinguishing them from non-islanding events like load switching or DG tripping. The flow chart of the proposed algorithm is shown in Fig. 4.

The hardware test setup, shown in Fig. 5 consists of hybrid $1-\phi$, 240 Vrms, 50 Hz, 3500 W grid-connected PV array. It includes 15 modules, each rated 250 Wp connected in series to produce up to 3750 Wp under standard test condition of 25 °C and 1000 W/m^2 solar irradiance. A single-phase DC/AC inverter is modelled using a PWM-controlled full-bridge MOSFET module (H-bridge). The filter topology follows a classical LCL configuration with $L_{grid} = L_{inv} = 4.366$ mH and $C_{fil} = 33$ uF. The inverter control comprises a MPPT controller based on the 'perturb and observe' technique, V_{DC} regulator, current regulator and PLL for synchronization. Based on the bipolar modulation

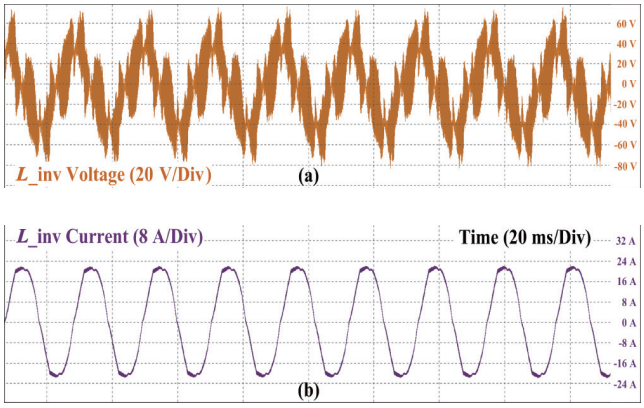

Fig. 6. Inverter-side inductor (a) voltage and (b) current waveform.

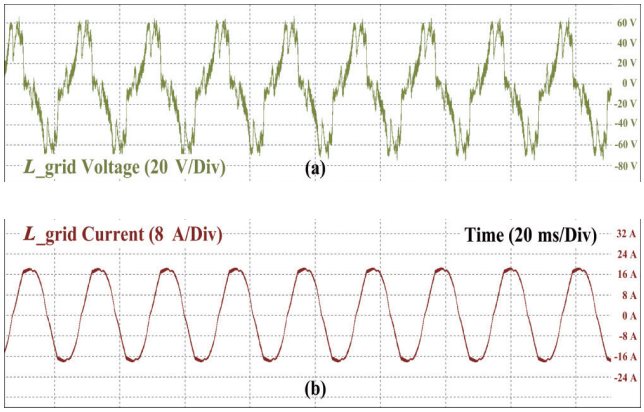

Fig. 7. Grid-side inductor (a) voltage and (b) current waveform.

method the PWM generator is utilized to generate pwm signals to the MOSFETs, with a carrier freqeuncy of 10000 Hz voltage and current signals are measured with a sampling frequency of 5 kHz i.e, 100 samples per cycle.

The voltage across the inverter side inductor L_{inv} and grid side inductor L_{grid} of the LCL filter, alone with the current through them, are measured as shown in Fig. 6(a) and (b) and Fig. 7(a) and (b) respectively. The *BH* curves are obtained over a moving window of one cycle using the mathematical formulae discussed in Section II. These curves are compared with the previous cycle *BH* curves successively to calculate correlation and alienation indices. The *BH* curves obtained from the inverter side and grid side inductors, one cycle before and after islanding are shown in Fig. 8(a) and (b) and Fig. 9(a) and (b) respectively. The variations in these curves are negligible to the naked eye. However the correlation (R_i *and* R_g) and alienation indices(A_i *and* A_g) exhibit significant changes following the islanding event after 1 s (50th cycle). The variation of the alienation indices for both inverter and grid side *BH* curves are shown in Fig. 10 and Fig. 11 respectively and the thresholds $T_{ai} = 0.62$ and $T_{ag} = 0.58$ are obtained by using the procedure explained in Section II. To detect islanding using alienation indices, the process approximately takes 6 cycles (120 ms) for inverter side measurements and 7 cycles (140 ms) for the grid side measurements. Since this method takes more time, anoth-

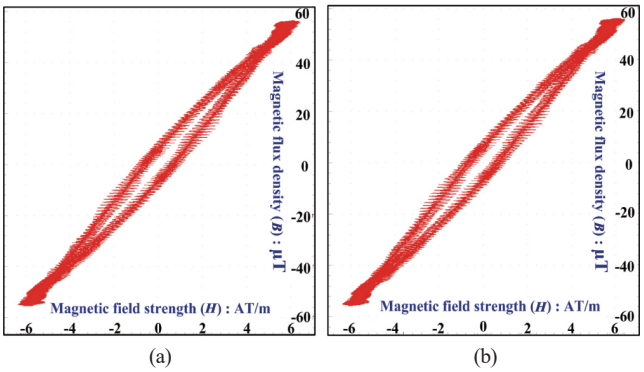

Fig. 8. Inverter-side BH curves (a) before and (b) after islanding.

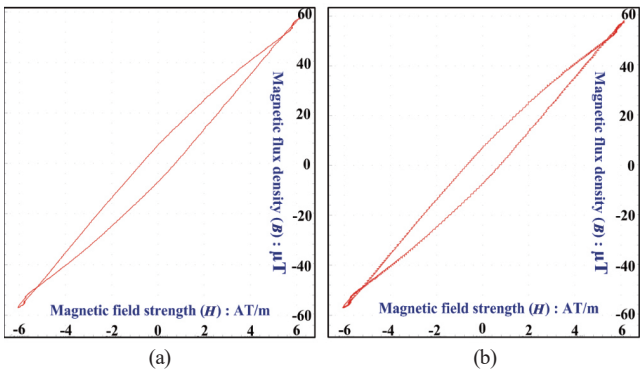

Fig. 9. Grid-side BH curves (a) before and (b) after islanding.

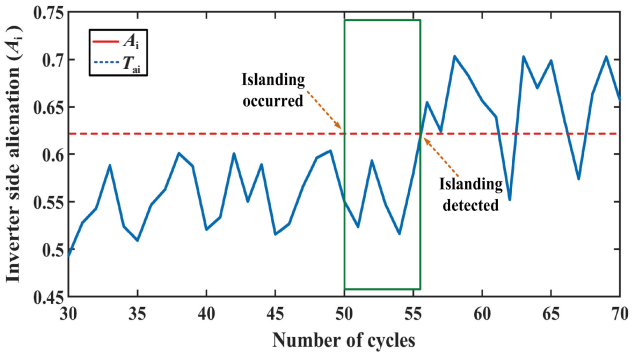

Fig. 10. Variation of alienation coefficients of inverter-side inductor measurements.

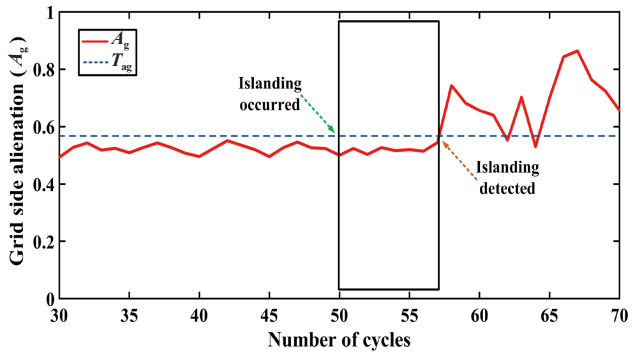

Fig. 11. Variation of alienation coefficients of grid-side inductor measurements.

er index is determined i.e., cumulative index (C_I), which is the product of N_i and N_g.

$$C_I = N_i \bullet N_g \tag{14}$$

The ratio of the square of the correlation coefficient to the alienation is computed for faster detection of the islanding given by

$$N_i = R_i^2 / A_i \tag{15}$$

where, R_i and A_i are the correlation and alienation indices for L_i. Similarly,

$$N_g = R_g^2 / A_g \tag{16}$$

The variation of the cumulative index (C_I) is shown in Fig. 12. The C_I is compared with the threshold $T_{CI} = 0.11$ to detect the islanding. The variations in cumulative indices are analysed for various case studies mentioned below.

IV. Results and Discussion

The performance of the algorithm is also validated by conducting hardware tests under various types of loads, including NDZ (non-detection zone) conditions. In these tests, RLC load parameters are selected to replicate a resonance condition. The changes in the active and reactive powers are analyzed within a range of −5% to +5%. As the power mismatch between the PV system and the load increases, the islanding detection process becomes more straightforward; therefore, a power mismatch of 5% is primarily considered. The system frequency is set to 50 Hz, and the measured signals are sampled at a frequency of 5 kHz. All disturbances are introduced at 1 second, with one event occurring at a time, ensuring non-simultaneous events. The hardware setup ensures that the information from the 51st cycle captures the impact of the disturbance. The variation in the cumulative index (C_I) is observed over a span of twenty cycles before and after the occurrence of an event, specifically from the 30th to the 70th cycle. These variations are documented and analyzed to verify the performance of the proposed algorithm.

A. Variation of Type of Disturbance

The proposed algorithm is evaluated by considering non-islanding events such as load switching and DG tripping. Improperly designed islanding detection algorithms may fail to filter transient disturbances, potentially triggering false islanding detection alarms. Sudden changes in grid parameters caused by load switching can erroneously activate the detection mechanism, resulting in unnecessary disconnection of the PV system from the grid. In the test scenario, load switching is introduced by opening a breaker at 1 s. The variation in the indices are shown in Fig. 13 ($\Delta P = \Delta Q = 0\%$). It is observed that the index increases after the load switching event remains

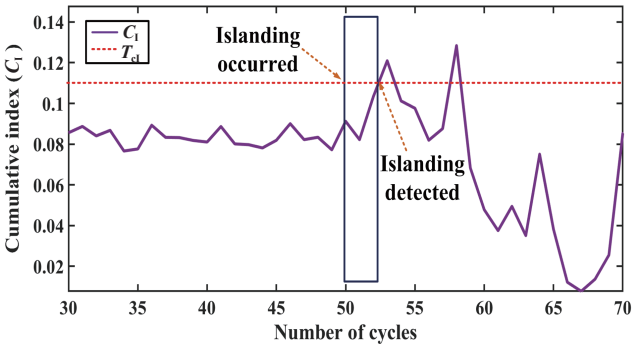

Fig. 12. Variation of cumulative index for islanding detection.

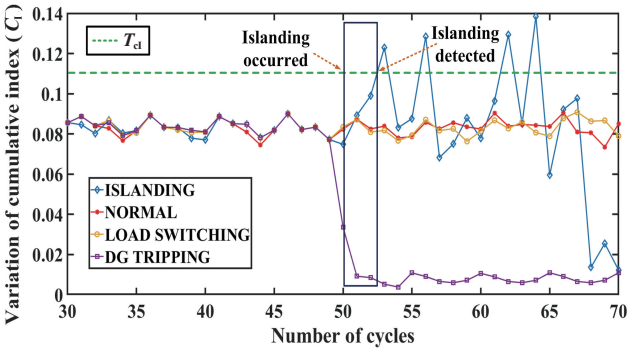

Fig. 15. Variation of cumulative index with type of disturbance (ΔP = 0% and ΔQ = −5%).

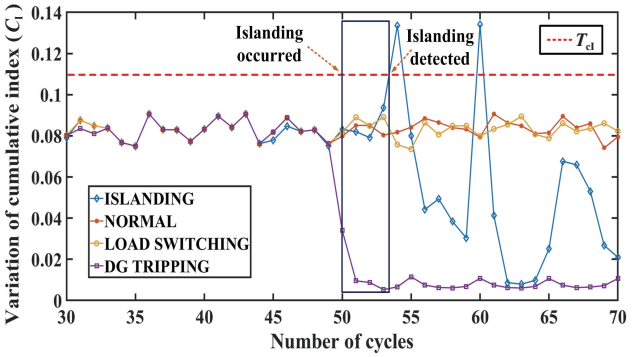

Fig. 13. Variation of cumulative index with type of disturbance ($\Delta P = \Delta Q$= 0%)

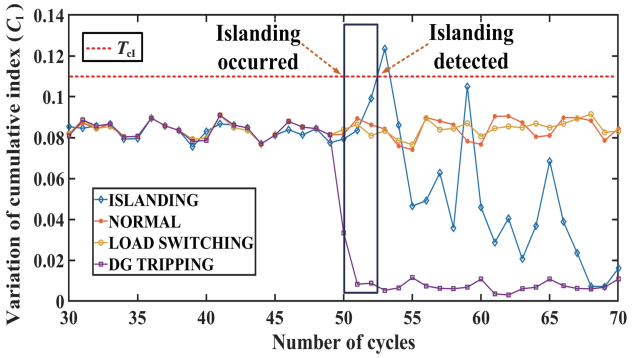

Fig. 16. Variation of cumulative index with type of disturbance (ΔP = +5% and ΔQ = 0%).

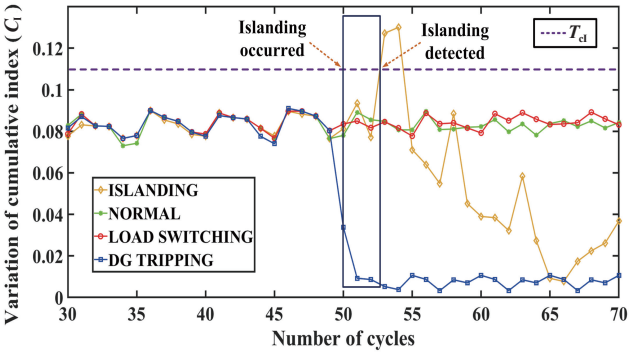

Fig. 14. Variation of cumulative index with type of disturbance (ΔP = 0% and ΔQ = +5%).

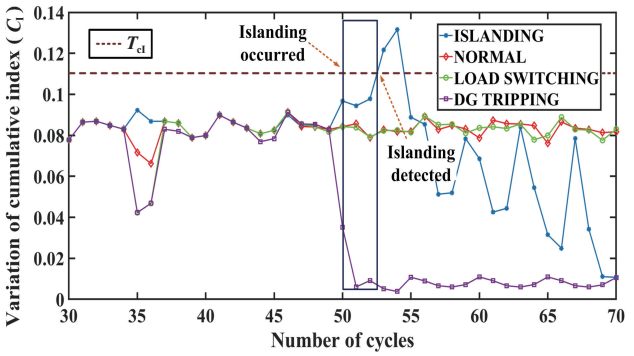

Fig. 17. Variation of cumulative index with type of disturbance (ΔP = −5% and ΔQ = 0%).

well within the threshold. After the tripping or disconnection of the solar inverter, the index decreased sharply. Notably, only actual islanding events result in the index exceeding the threshold, facilitating straightforward detection when the load is a parallel RLC load. The variations of the cumulative indices under different power mismatch conditions such as ΔP = 0% and ΔQ = +5% , ΔP = 0% and ΔQ = −5% , ΔP = +5% and ΔQ = 0% and ΔP = −5% and ΔQ = 0% are shown in Figs. 14 − 17, respectively.

B. Variation of Type of Load

The proposed algorithm is tested by changing the type of the loads. Three load combinations, such as RLC, RL and RC are considered to replicate resonance condition, positive reactive power, and negative reactive power respectively. The values of R = 15.11 Ω, L = 48.86 mH and C = 210 μF are chosen. The variation in the indices are shown in Fig. 18. It can be observed that the proposed algorithm successfully detects islanding in the presence of all types of load combinations.Additionally, the detection time is longer for RLC load when compared to RL and RC loads due to resonance.

C. Variation of Active and Reactive Power Mismatch

The proposed algorithm is tested as per the IEC 62116 standard, which accounts for active and reactive power mismatches. Under normal conditions, power discrepancies are balanced by the grid. However, when the grid is disconnected

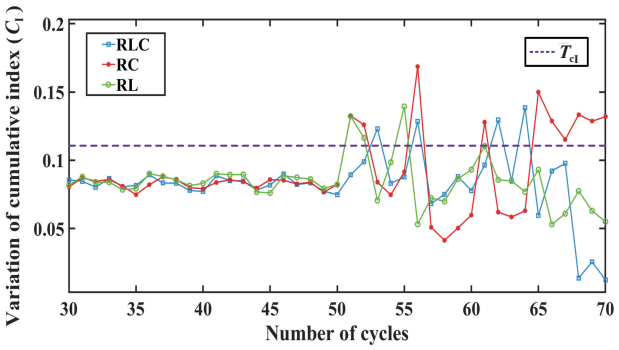

Fig. 18. Variation of cumulative index with type of load.

TABLE II
DETECTION TIME IN CYCLES FOR VARIOUS INDICES PROPOSED

Power mismatch	A_i coefficient	A_g coefficient	C_I index
$\Delta P = 0\%$, $\Delta Q = 0\%$	6	7	3
$\Delta P = +5\%$, $\Delta Q = 0\%$	4	4	2
$\Delta P = -5\%$, $\Delta Q = 0\%$	4	4	2
$\Delta P = 0\%$, $\Delta Q = +5\%$	4	3	2
$\Delta P = +5\%$, $\Delta Q = +5\%$	3	3	2
$\Delta P = -5\%$, $\Delta Q = +5\%$	4	5	2
$\Delta P = 0\%$, $\Delta Q = -5\%$	6	7	2
$\Delta P = +5\%$, $\Delta Q = -5\%$	4	5	3
$\Delta P = -5\%$, $\Delta Q = -5\%$	3	4	2

in islanding mode, changes in active power are reflected as voltage fluctuations, while changes in reactive power manifest as over/under frequency deviations. The worst-case scenario arises when the active and reactive powers of the load and the inverter are perfectly matched, a condition referred to as the non-detection zone (NDZ). Under this scenario, the differences in active and reactive power are $\Delta P = P_{inv} - P_{load} = 0$ and $\Delta Q = Q_{inv} - Q_{load} = 0$. The values of $R = 15.11\ \Omega$, $L = 48.86$ mH and $C = 210\ \mu$F are chosen to obtain the resonance condition at 50 Hz for the inverter capacity of 3.5 kVA. An incremental variations in active and reactive powers are maintained as + or −5% along with the NDZ condition. The time of detection is enumerated in the Table II. It can be observe that the proposed cumulative index demonstrates shorter average detection times compared to either the grid-side alienation index or the inverter-side alienation index when evaluated independently.

The detection time of the proposed algorithm is evaluated against various international standards. It is observed that the detection time is below the minimum of 0.2 s according to Table II. Using the cumulative index the detection can be achieved in less than 3 cycles for NDZ.

V. CONCLUSION

The *BH* curves are effectively utilized for detecting islanding event and distinguished them from other non-islanding switching events, such as load switching and DG disconnection. The voltage and current signals across and through the both inverter and grid-side inductors of the LCL filter are employed to obtain the *BH* curves.These *BH* curves are continuously compared cycle by cycle to produce an alienation coefficient vectors on grid side and inverter side. The maximum time of detection by grid side inductor measurements is 7 cycles, while it is reduced to 6 cycles for inverter side inductor. Furthermore, the cumulative index successfully detected the islanding event within less than or equal to 3 cycles. The proposed method remains effective even when voltage and power remain constant, as the magnetic response of the LCL filter inductors changes due to the loss of the grid's influence. The alienation coefficient (A) and cumulative index (C_I) quantify subtle shifts in the *BH* curve caused by variations in system impedance and harmonic content. Since the grid serves as a stiff voltage source, its disconnection results in a detectable shift in inductance behavior, allowing islanding detection even in perfectly matched load conditions.

REFERENCES

[1] R. Bakhshi-Jafarabadi, J. Sadeh, A. Serrano-Fontova, and E. Rakhshani, "Review on islanding detection methods for grid-connected photovoltaic systems, existing limitations and future insights," in *IET Renewable Power Generation*, vol. 16, no. 15, pp. 3406–3421, Jul. 2022.

[2] "IEEE standard for interconnection and interoperability of distributed energy resources with associated electric power systems interfaces," in *IEEE Std 1547-2018 (Revision of IEEE Std 1547-2003)*, pp.1–138, Apr. 2018.

[3] Y. -K. Wu, J. -H. Lin, and H. -J. Lin, "Standards and guidelines for grid-connected photovoltaic generation systems: A review and comparison," in *IEEE Transactions on Industry Applications*, vol. 53, no. 4, pp. 3205–3216, Jul.-Aug. 2017.

[4] K. N. E. K. Ahmad, J. Selvaraj, and N. Abd Rahim, "A review of the islanding detection methods in grid-connected PV inverters," in *Renewable and Sustainable Energy Reviews*, vol. 21, pp. 756–766, May 2013.

[5] M. A. Khan, A. Haque, V. B. Kurukuru, and M. Saad, "Islanding detection techniques for grid-connected photovoltaic systems-A review," in *Renewable and Sustainable Energy Reviews*, vol. 154, p. 111854, Feb. 2022.

[6] Ê. C. Resende, M. G. Simões, and L. C. G. Freitas, "Anti-islanding techniques for integration of inverter-based distributed energy resources to the electric power system," in *IEEE Access*, vol. 12, pp. 17195–17230, 2024.

[7] H. Khosravi, H. Samet, and M. Tajdinian, "Robust islanding detection in microgrids employing rate of change of kinetic energy over reactive power," in *IEEE Transactions on Smart Grid*, vol. 13, no. 1, pp. 505–515, Jan. 2022.

[8] A. Serrano-Fontova, J. A. Martinez, P. Casals-Torrens, and R. Bosch, "A robust islanding detection method with zero-non-detection zone for distribution systems with DG," in *International Journal of Electrical Power & Energy Systems*, vol. 133, p. 107247, Dec. 2021.

[9] R. Nale, M. Biswal, and N. Kishor, "A passive communication based islanding detection technique for AC microgrid," in *International Journal of Electrical Power & Energy Systems*, vol. 137, p. 107657, May 2022.

[10] G. Song, B. Cao, and L. Chang, "A passive islanding detection method for distribution power systems with multiple inverters," in *IEEE Journal of Emerging and Selected Topics in Power Electronics*, vol. 10, no. 5, pp. 5727–5737, Oct. 2022.

[11] M. Tajdinian, H. Khosravi, H. Samet, and Z. M. Ali, "Islanding detection scheme using potential energy function based criterion," in *Electric Power Systems Research*, vol. 209, p. 108047, Aug. 2022.

[12] M. W. Altaf, M. T. Arif, S. Saha, S. N. Islam, M. E. Haque, and A. M. T. Oo, "Effective ROCOF-based islanding detection technique for different

types of microgrid," in *IEEE Transactions on Industry Applications*, vol. 58, no. 2, pp. 1809–1821, Mar.-Apr. 2022.

[13] Z. S. Chafi, H. Afrakhte, and A. Borghetti, "μPMU-based islanding detection method in power distribution systems," in *International Journal of Electrical Power & Energy Systems*, vol. 151, p. 109102, Spet. 2023.

[14] M. Shaik, S. K. Yadav, and A. G. Shaik, "Distribution feeder protection using uncorrelated symmetrical dot patterns," in *TENCON 2019-2019 IEEE Region 10 Conference (TENCON)*, Kochi, India, 2019, pp. 1875–1880.

[15] P. Ramesh and S. Nadig, "Measurement of inductance using a digital storage oscilloscope under real-time operating environments," U.S. Patent 6876936. Apr. 5, 2005.

Shanthi Kumar N B received his B.Tech. degree in Electrical and Electronics Engineering from KSRM College of Engineering, Kadapa, India, in 2020. He is currently pursuing a Ph.D. in solar photovoltaic systems and power electronics at Mahindra University, Hyderabad, India. His research interests include fault detection, mitigation in SPV systems, and on-grid implementation.

Sreedhar Madichetty received his B.Tech. degree from JNTU, Anantapur, in 2010, and M.Tech. and Ph.D. from KIIT University, Bhubaneswar, in 2012 and 2015, respectively. He served as a lecturer at BITS Pilani (2014), an SERB-sponsored NPDF at IIT Delhi (2017), and a Senior Research Fellow at Trinity College Dublin (2019). Currently he is a Professor at Mahindra University, Hyderabad, he is a senior IEEE member with 50+ publications, focusing on power electronics, cyber-physical systems, and renewable energy.

Chandrakala Pannela received her B.Tech. degree in Electrical and Electronics Engineering from SVIST, Kadapa, India, in 2023. She is currently pursuing a Master's degree in the department of Electrical and Computer Engineering at Mahindra University, Hyderabad, India, specializing in Autonomous Electrical Vehicles Engineering. Her research interests include grid-tied inverters, and solar photovoltaic systems.

Pradeep Kumar is currently working as a National Post Doctoral Fellow Sponsored by ANRF Govt of India at the Department of Electrical and Computer Engineering at Mahindra University, Hyderabad, India, specializing in Autonomous Electrical Vehicles Engineering. Her research interests include grid-tied inverters, and solar photovoltaic systems.

Mahmood Shaik received his Ph.D. degree from Indian Institute of Technology Jodhpur (IIT Jodhpur) in 2023 in Electrical Engineering. He was associated with Mahindra University, Hyderabad as a post doctoral researcher. His research includes signal processing and AI applications for power quality assessment, protection of the distribution system in the presence of renewable energy sources.